Topological Bloch bands in graphene superlattices

Justin C. W. Song[a,b,c,1], Polnop Samutpraphoot[c], and Leonid S. Levitov[c,1]

[a]Walter Burke Institute for Theoretical Physics, California Institute of Technology, CA 91125; [b]Institute for Quantum Information and Matter, and Department of Physics, California Institute of Technology, CA 91125; and [c]Department of Physics, Massachusetts Institute of Technology, Cambridge, MA 02139

Edited by Subir Sachdev, Harvard University, Cambridge, MA, and approved June 24, 2015 (received for review December 30, 2014)

We outline a designer approach to endow widely available plain materials with topological properties by stacking them atop other nontopological materials. The approach is illustrated with a model system comprising graphene stacked atop hexagonal boron nitride. In this case, the Berry curvature of the electron Bloch bands is highly sensitive to the stacking configuration. As a result, electron topology can be controlled by crystal axes alignment, granting a practical route to designer topological materials. Berry curvature manifests itself in transport via the valley Hall effect and long-range chargeless valley currents. The nonlocal electrical response mediated by such currents provides diagnostics for band topology.

topological bands | graphene | van der Waals heterostructure

Electronic states in topological materials possess unique properties including a Hall effect without an applied magnetic field (1–3) and topologically protected edge states (4, 5). Accessing nontrivial electron topology depends on identifying materials in which symmetry and interactions produce topological Bloch bands. Such bands can only arise when multiple requirements, such as a multiband structure with a Berry phase and suitable symmetry, are fulfilled. As a result, topological bands are found in only a handful of exotic materials in which good transport properties are often lacking. Formulating practical methods for transforming widely available materials with a reasonably high carrier mobility (such as silicon or graphene) into a topological phase remains a grand challenge.

Here, we lay out an approach for engineering designer topological materials out of stacks of generic materials—"Chernburgers." Our scheme naturally produces (*i*) topological bands with different Chern invariant values, and (*ii*) tunable topological transitions. As an illustration, we analyze graphene on hexagonal boron–nitride heterostructures (G/*h*BN), where broken inversion symmetry is expected to generate Berry curvature (6, 7), a key ingredient of topological materials. Indeed, recently valley currents have been demonstrated in a G/*h*BN system (8) signaling the presence of Berry curvature (6). As we will show, Berry curvature in G/*h*BN can be molded by stacking configuration, leading to a large variability in properties. Transitions between different topological states can be induced by a slight change in stacking angle.

Topological bands in G/*h*BN arise separately for valley K and valley K'. Graphene bandstructure reconstruction due to the coupling to *h*BN produces superlattice minibands (9–14), with Berry curvature $\Omega(\mathbf{k})$ developing near avoided crossings. The minibands for each valley possess a valley Chern number

$$\mathcal{C}_v = \frac{1}{2\pi} \int_{k\in \mathrm{SBZ}} d^2k \Omega(\mathbf{k}), \qquad [1]$$

where the integral is taken over the entire superlattice Brillouin zone (SBZ) in one valley (K or K'). As discussed below, for commensurate stackings (Fig. 1*A*) $\mathcal{C}_v = \pm 1$ for the lowest minibands. In contrast, for incommensurate moiré superlattice structures (Fig. 1*B*), the invariant [**1**] vanishes in these minibands, $\mathcal{C}_v = 0$. The difference in the behavior for these configurations arises from the difference in sign of the contributions to Berry curvature from regions near SBZ center $\tilde{\Gamma}$ (the Dirac point, hereafter denoted DP) and corners $\tilde{K}$, $\tilde{K}'$ (Fig. 2). We will see that these contributions add in the commensurate case but subtract for the incommensurate case, yielding topological and nontopological bands, respectively (Fig. 1).

Interestingly, the conditions for both topological and nontopological bands are met by currently available systems. Indeed, both commensurate and incommensurate stackings have been recently identified in G/*h*BN by scanning probe microscopy (15, 16). Further, the commensurate–incommensurate transition can be controlled by twist angle between G and *h*BN, providing a practical route in which to tailor electron topology via a tunable structural transition.

We note that time-reversal (TR) symmetry requires that $\Omega(\mathbf{k})$ in K and K' valleys have opposite signs. As a result, the total Chern invariant always vanishes, $\mathcal{C}_v(K) + \mathcal{C}_v(K') = 0$. However, the weakness of intervalley scattering (17, 18) can enable long-range topological currents in individual valleys. As we will see, the nonlocal electrical signals mediated by such currents can provide diagnostics for valley band topology.

We also note that topological bands in graphene are sometimes presumed either impossible or impractical. Indeed, a connection between K and K' bands at high energies, whenever present, renders valley-specific topological invariants ill-defined (19, 20). Proposals relying on large spin–orbit coupling (21, 22) are also sensitive to disorder; proposals in other systems such as optical flux lattices (23) suffer from similar implementation pitfalls. Our scheme circumvents these difficulties by exploiting Bragg scattering in the G/*h*BN superlattice to create energy gaps above and below the K and K' Dirac points (Fig. 2). The Dirac points, sandwiched between these gaps, are no longer connected in a single band; the resulting minibands possess well-defined topological invariants.

Minimal Model for Superlattice Bands

Modeling the superlattice bandstructure is greatly facilitated by several aspects of the G/*h*BN system. First is the long-wavelength character of superlattice periodicity, which results from nearly identical periods of graphene and *h*BN crystal structure. For

Significance

A family of designer topological materials is introduced, comprising stacks of two-dimensional materials which by themselves are not topological, such as graphene. Previously, topological bands in graphene were presumed either impossible or impractical. The designer approach turns graphene into a robust platform with which a host of topological behavior can be realized and explored.

Author contributions: J.C.W.S. and L.S.L. designed research; J.C.W.S., P.S., and L.S.L. performed research; and J.C.W.S. and L.S.L. wrote the paper.

The authors declare no conflict of interest.

This article is a PNAS Direct Submission.

[1]To whom correspondence may be addressed. Email: justin.song.cw@gmail.com or levitov@mit.edu.

This article contains supporting information online at www.pnas.org/lookup/suppl/doi:10.1073/pnas.1424760112/-/DCSupplemental.

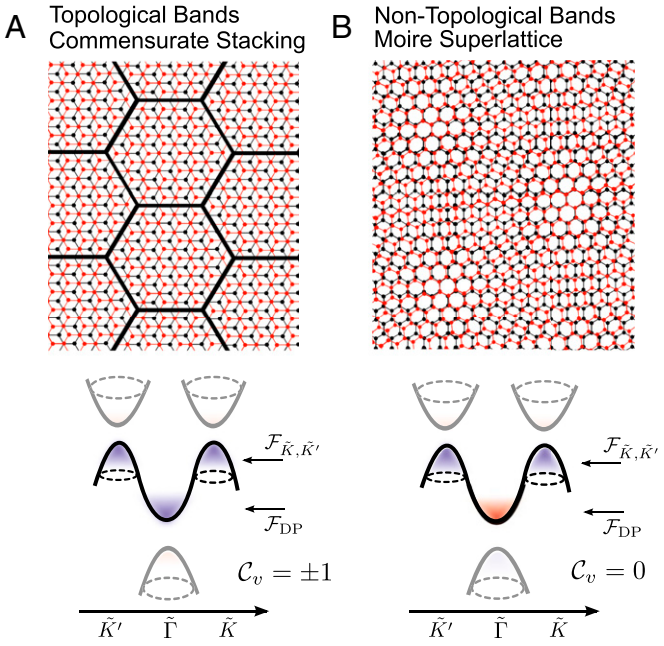

Fig. 1. Topology of Bloch bands for different stacking types of G/*h*BN, commensurate (*A*) and incommensurate (*B*). (*Top*) Hexagonal commensurate domains (black lines mark domain walls) and incommensurate moiré superlattice structure. (*Bottom*) Valley Chern number $\mathcal{C}_v = \pm 1$ and $\mathcal{C}_v = 0$ for the lowest reconstructed minibands labeled "1" in Fig. 2. This corresponds to the contributions to the net Berry flux, $\mathcal{F} = \mathcal{F}_{\rm DP} + \mathcal{F}_{\tilde{K},\tilde{K}'}$, from the superlattice Brillouin zone center $\tilde{\Gamma}$ and corners $\tilde{K}$, $\tilde{K}'$ that have equal signs and opposite signs, respectively (see Eqs. **12** and **13**). Red and blue shaded regions indicate the "+" and "−" signs of Berry curvature.

commensurate stackings, the superlattice structure is defined by a periodic array of hexagonal domains (Fig. 1*A*). Its periodicity, which is set by the size of the domains, is on the order of $\lambda \approx 100$ atomic distances. Likewise, in incommensurate stackings (Fig. 1*B*) the lattice mismatch and the twist angle between graphene and *h*BN produce long-period moiré patterns with wavelength $\lambda \approx 10$ nm. Because the corresponding superlattice wavevector $b = 2\pi/\lambda$ is too small to produce Bragg scattering between valleys K and K', the bandstructure reconstruction can be understood in terms of a Dirac model, giving an SBZ minibandstructure separately for the K and K' valleys (Fig. 2) (9–14, 24, 25).

Another property of the G/*h*BN system that simplifies modeling is a relatively weak coupling strength. Indeed, the reported values for the *h*BN-induced energy gap at the Dirac point are on the order of 500 K (8, 16, 26), which is about 10 times smaller than the energy $\epsilon_0 = \hbar v b$, where b is the superlattice wavevector and $v = 10^6$ m/s. This disparity allows one to describe the superlattice bandstructure, for both commensurate and incommensurate stackings, with the effective Hamiltonian

$$H = v\boldsymbol{\sigma}\cdot\mathbf{p} + \Delta(\mathbf{r})\sigma_3, \quad \Delta(\mathbf{r}) = \Delta_{\rm g} + m_3\sum_{j=1}^{3}\cos(\mathbf{b}_j\cdot\mathbf{r}), \qquad [2]$$

where $\Delta(\mathbf{r})$ accounts for the coupling between graphene and *h*BN. Our minimal model, given in Eq. **2**, is sufficient to understand the key features of the bandstructure for both stacking types. In particular, $\Delta_{\rm g}$ describes the global gap at DP (point Γ), whereas m_3 describes Bragg scattering that creates avoided crossings at $\tilde{K}$ and $\tilde{K}'$ (Fig. 2). As a result, the minibands are distinct and separated by energy gaps disconnecting the original K and K' points. Our microscopic analysis, presented below, indicates that the terms $\Delta_{\rm g}$ and m_3 are present for both commensurate and incommensurate stackings. Crucially, the two cases are distinguished by opposite relative signs of $\Delta_{\rm g}$ and m_3. This sign difference, as we will see, is key in producing different topological classes.

We note parenthetically that a more general Hamiltonian can also include a scalar potential term modulated in the same way as the σ_3 term above (9, 10, 13). However, as discussed elsewhere (14) the electron interaction effects strongly enhance the σ_3 coupling, but leave the scalar potential unrenormalized. Hence, we take the σ_3 term as the dominant part of superlattice potential ignoring the scalar potential contribution. On similar grounds we disregard possible modulation of σ_1 and σ_2 types that may arise due to strain.

Global Gap and the Signs of $\Delta_{\rm g}$ and m_3

Turning to the analysis of the coupling in Eq. **2**, we first consider the commensurate case, where all of the hexagonal domains adopt the same lowest energy atomic configuration. The simplest arrangement to produce such a stacking is perfect crystal axes alignment when G and *h*BN lattices conform with each other as pictured in Fig. 1*A*. While we have used AB stacking where G and *h*BN crystal axes are aligned in our illustration in Fig. 1*A*, other stackings can also be used, yielding similar results. Other commensurate stackings in the absence of perfect crystal axes alignment may also occur and do not affect our main conclusions. The registration within each hexagonal cell is locked, producing an A/B sublattice asymmetry in graphene. Crucially, the sign of this asymmetry cannot change upon lateral sliding which is not accompanied by a rotation. Hence the asymmetry is of the same sign throughout the structure, leading to a global constant-sign gap.

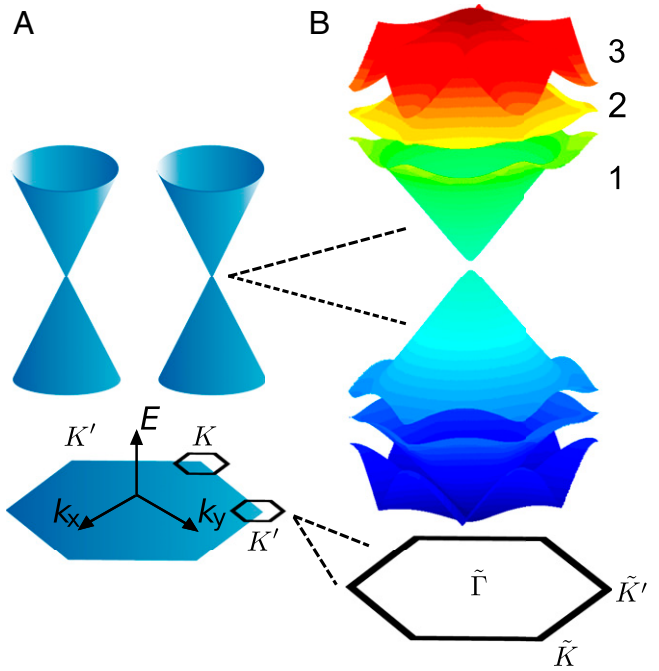

Fig. 2. Graphene superlattice potential transforms the massless Dirac bandstructure near points K, K' of graphene Brillouin zone (*A*) into a family of minibands (*B*). Shown is the bandstructure near points K, K' obtained from the Hamiltonian in Eq. **2** (parameters used: $m_3 = 60$ meV, $\epsilon_0 = \hbar v|\mathbf{b}| = 1$ eV, $\Delta_{\rm g} = 20$ meV). Large superlattice period translates into a small size of superlattice Brillouin zones (two hexagons positioned at points K, K'). Sublattice A/B dependent coupling (σ_3 term in Eq. **2**) generates a Dirac mass term and opens a gap between the conduction and valence bands; it also creates avoided band crossings 1–2–3 above and below Dirac points.

To illustrate this important point, we present the argument in a form that does not depend on detailed knowledge of the registration within each of the domains. Of course, in practice the registration types (and hence the asymmetry signs) arise from general energetic and geometric constraints which can be easily accounted for (27). As an example, we consider three possible registrations: (*i*) site A in *h*BN aligned with site A in graphene and site B in *h*BN with site B in graphene; (*ii*) site A in *h*BN aligned with site B in graphene and site B in *h*BN with H (hollow) in graphene; and (*iii*) A in *h*BN aligned with site B in graphene whereas site B in *h*BN aligned with site A in graphene.

Configurations (*i*) and (*iii*) cost the same energy, but have a different energy than (*ii*). Importantly, lateral sliding of a cell with configuration (*i*) cannot generate configuration (*iii*) because it would require a lattice rotation. At the same time, whereas lateral sliding of a cell with configuration (*i*) can generate configuration (*ii*), it costs a different energy. As a result, stacking frustration between neighboring cells cannot occur, locking the registration between all hexagonal cells to yield a constant global gap, Δ_g.

Next, we note that imperfect registration around the domain boundaries yields a weaker coupling between G and *h*BN [strained graphene sheet buckles (16) increasing the G-to-*h*BN distance]. Reduction in sublattice-asymmetric potential $\Delta_{g,0}$ can be modeled as

$$\Delta(\mathbf{r}) = \Delta_{g,0} + \delta m[G(\mathbf{r}) * F(\mathbf{r})], \quad \text{sgn}\,\delta m = -\text{sgn}\,\Delta_{g,0}, \qquad [3]$$

where $F(\mathbf{r})$ describes the unit cell of the pattern of domain walls, $G(\mathbf{r}) = \sum_{n,l\in Z}\delta(\mathbf{r} - n\mathbf{a}_1 - l\mathbf{a}_2)$ is the superlattice form factor ($\mathbf{a}_{1,2}$ are superlattice basis vectors), and * indicates convolution. The relative sign sgn $\delta m = -$sgn Δ_g accounts for the weaker coupling between G and *h*BN at the domain boundaries.

Because we are interested in bandstructure reconstruction in the lowest minibands, we expand $\Delta(\mathbf{r})$ into lowest harmonics yielding Eq. **2** with

$$\Delta_g = \Delta_{g,0} + \delta m\tilde{F}_{\mathbf{q}=0}, \quad m_3 = 2\delta m\tilde{F}_{\mathbf{q}=\mathbf{b}_j}, \qquad [4]$$

where $\tilde{F}(\mathbf{q}) = 1/\mathcal{A}\int d^2\mathbf{r}F(\mathbf{r})e^{i\mathbf{q}\cdot\mathbf{r}}$ is the form factor, $\mathbf{b}_j$ are the reciprocal superlattice vectors, and $\mathcal{A}$ is the area of superlattice unit cell. Crucially, the sign of the form factor F determines the sign of m_3. Choosing a symmetric $F(\mathbf{r})$, with origin at the center of a hexagonal domain (pictured in Fig. 1*A*, $\hat{\mathbf{x}}$ and $\hat{\mathbf{y}}$ are the horizontal and vertical directions) and δ-functions along the hexagonal domain walls, we obtain the form factor

$$\tilde{F}(\mathbf{q}) = \frac{2w}{\mathcal{A}}\sum_{j=1}^{3}\frac{\sin\left(\frac{d}{2}\mathbf{q}_i\cdot\hat{\mathbf{x}}\right)}{\mathbf{q}_i\cdot\hat{\mathbf{x}}}\cos\left(\frac{\sqrt{3}d}{2}\mathbf{q}_i\cdot\hat{\mathbf{y}}\right). \qquad [5]$$

Here d and w are the domain wall length and width, and $\mathbf{q}_i = R(\theta_j)\mathbf{q}$, where $R(\theta_j)$ are the 2×2 rotation matrices with $\theta_1 = 0$, $\theta_2 = \pi/3$, and $\theta_3 = 2\pi/3$.

Evaluating Eq. **5** gives $\tilde{F}_{\mathbf{q}=0} = 3\zeta > 0$ and $\tilde{F}_{\mathbf{q}=\mathbf{b}_j} = -9\sqrt{3}\zeta/4\pi < 0$, where $\zeta = wd/\mathcal{A} > 0$. Comparing with Eq. **2**, we find the relation between signs of m_3 and Δ_g:

$$\text{sgn}\,m_3 = -\text{sgn}(\delta m) = \text{sgn}(\Delta_g). \qquad [6]$$

As we will see, this leads to a nontrivial topological class $\mathcal{C}_v = \pm1$ in the lowest minibands (Fig. 3*A*).

The incommensurate case (moiré superlattice) differs from the commensurate case in two important ways. One is that the G-to-*h*BN coupling is dominated by the modulational part $\Delta(\mathbf{r}) = m_3\sum_{j=1}^{3}\cos(\mathbf{b}_j\cdot\mathbf{r})$ arising from the moiré pattern. The other is that the global gap parameter Δ_g is zero in the bare

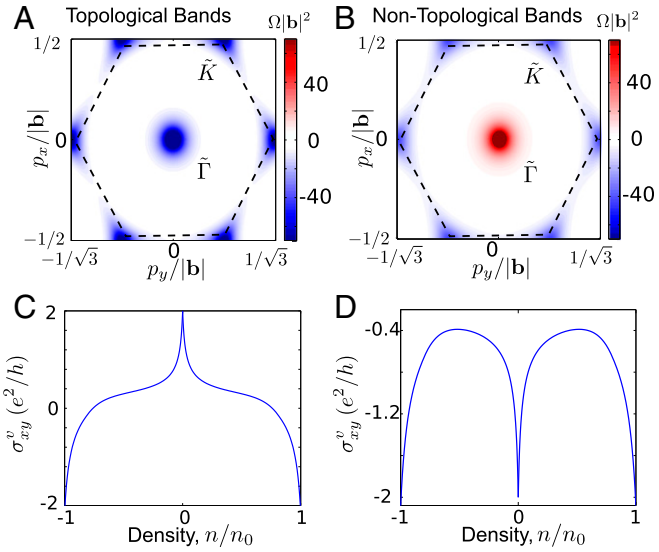

Fig. 3. (*A* and *B*) Berry curvature distribution, $\Omega(\mathbf{k})$, in the lowest conduction band (labeled "1" in Fig. 2*B*) obtained from the Hamiltonian in Eq. **2**. Two choices of signs, (*A*) $\text{sgn}(\Delta_g) = \text{sgn}(m_3)$ and (*B*) $\text{sgn}(\Delta_g) = -\text{sgn}(m_3)$, yield $\mathcal{C}_v = -1$ and $\mathcal{C}_v = 0$, respectively. The hot spots of $\Omega(\mathbf{k})$ at DP (point $\tilde{\Gamma}$) and SBZ corners $\tilde{K}$, $\tilde{K}'$ correspond to gap opening and avoided band crossing regions. The central hot spot carries a net Berry flux π, whereas the corner hot spots carry a net flux $\pm\pi/2$ (see the text). Parameters used: $m_3 = 20$ meV, $\epsilon_0 = \hbar v|\mathbf{b}| = 300$ meV, $\Delta_g = m_3$ in *A*; $\Delta_g = -m_3$ in *B*. (*C* and *D*) Valley Hall conductivity, σ^v_{xy} (Eq. **14**), vs. carrier density for the two minibands above and below DP: σ^v_{xy} changes sign for topological bands (*C*) but keeps the same sign for nontopological bands (*D*) (n_0 is the density needed to fill the first miniband, other parameter values are the same as in *A* and *B*).

Hamiltonian; however, a nonzero Δ_g value is generated perturbatively in m_3, with the Δ_g sign the opposite of the m_3 sign. The analysis is particularly simple for the long-period moiré patterns arising for rigid G and *h*BN stackings at small twist angles, as shown in Fig. 1*B*.

Of course, one m_3 harmonic cannot produce an average global gap at DP because it is sign-changing, $\langle e^{i\mathbf{bx}}\rangle = 0$. However, a combination of three different harmonics can open up a gap (14). This can be seen from a perturbation analysis of the Hamiltonian [**2**] which we write as $H = H_0 + V$, where $H_0 = v\boldsymbol{\sigma}\cdot\mathbf{p}$, $V = \sigma_3 m_3\sum_{j=1}^{3}\cos(\mathbf{b}_j\cdot\mathbf{r})$. Perturbation theory in V yields a term describing a global gap at a third order in V via

$$\delta H = V\frac{1}{\epsilon - H_0}V\frac{1}{\epsilon - H_0}V. \qquad [7]$$

Choosing triplets of harmonics with $\mathbf{b}_i + \mathbf{b}_j + \mathbf{b}_k = 0$, third-order perturbation theory in m_3 yields a gap

$$\Delta_g = \sum_{\pm\mathbf{b}_i,\pm\mathbf{b}_k}\frac{m_3\sigma_3}{2}\frac{1}{v\boldsymbol{\sigma}\cdot\mathbf{b}_i}\frac{m_3\sigma_3}{2}\frac{1}{v\boldsymbol{\sigma}\cdot\mathbf{b}_k}\frac{m_3}{2} = -\frac{3m_3^3}{4(v|\mathbf{b}|)^2}, \qquad [8]$$

where the minus sign results from the anticommutation relations $[\sigma_1,\sigma_3]_+ = 0$, $[\sigma_2,\sigma_3]_+ = 0$. Importantly, this analysis predicts a relation between signs

$$\text{sgn}(\Delta_g) = -\text{sgn}(m_3), \qquad [9]$$

which is opposite to the relation found for the commensurate case, Eq. **6**. Whereas the gap size obtained at a third order of perturbation theory in a noninteracting system is small, electron interaction effects are expected to produce an enhancement and

PHYSICS

generate a large Δ_g (14). As we will see, the signs in Eq. **9** lead to trivial topological classes for superlattice bands, $\mathcal{C}_v = 0$ (Fig. 3*B*).

In addition to the difference in signs, the commensurate and incommensurate stackings differ in the relative magnitude of the Δ_g and m_3 couplings. As we argued above, the global gap coupling Δ_g dominates in the commensurate case, with a relatively weaker modulational part m_3 arising due to registration unzipping along domain boundaries. In contrast, the modulational coupling m_3 is dominant in the incommensurate case, with the global gap Δ_g arising at third-order perturbation in m_3. The two distinct microscopic pictures result in a disparity between the Δ_g and m_3 scales and a sign difference, ultimately leading to different topological classes.

Topological Classes

We proceed to explore how stacking types impact the band topology. The topological properties of G/*h*BN can be analyzed through the Berry curvature in the minibands. Even though the G/*h*BN Hamiltonian, Eq. **2**, possesses TR symmetry, its broken inversion symmetry allows for a finite Berry curvature to develop in the SBZ:

$$\Omega_n(\mathbf{k}) = \nabla_{\mathbf{k}} \times \mathbf{A}_n(\mathbf{k}), \quad \mathbf{A}_n(\mathbf{k}) = i\langle u_n(\mathbf{k})|\nabla_{\mathbf{k}}|u_n(\mathbf{k})\rangle. \qquad [10]$$

Here n is the band index, $\mathbf{A}$ is the Berry connection, and $|u_n(\mathbf{k})\rangle$ are the eigenvectors of Eq. **2**. In what follows, we concentrate on a single valley and the lowest conduction miniband (labeled "1" in Fig. 2*B*).

Using Eq. **10**, we evaluate $\Omega_n(\mathbf{k})$ for the bandstructure generated by Eq. **2**, and obtain Berry curvature maps in SBZ reciprocal space which are shown in Fig. 3 *A* and *B*. We adopted a numerical method similar to that outlined in ref. 28; see the *Supporting Information* for a full description. In Fig. 3 *A* and *B* we plot $\Omega(\mathbf{k})$ corresponding to the lowest conduction band (labeled "1" in Fig. 2*B*); the lowest valence band exhibits the same behavior but with opposite sign. We find that $\Omega(\mathbf{k})$ is concentrated in the reciprocal space regions where the bandstructure exhibits gaps and avoided crossings, namely at the Dirac points and SBZ corners [$\tilde{\Gamma}$, and $\tilde{K}$, $\tilde{K}'$ respectively].

Integrating $\Omega(\mathbf{k})$ over the superlattice Brillouin zone to obtain the valley Chern number, Eq. **1**, we identify two distinct cases. For the equal-sign case, Eq. **6**, which corresponds to commensurate stackings, we obtain $\mathcal{C}_v = -1$ (Fig. 3*A*). For the opposite-sign case, Eq. **9**, which corresponds to incommensurate stackings, we obtain $\mathcal{C}_v = 0$ (Fig. 3*B*). This gives topological and nontopological bands, respectively.

To gain more insight into band topology in Fig. 3, it is instructive to analyze the hot spots of $\Omega(\mathbf{k})$ individually. Near SBZ center $\tilde{\Gamma}$, the bandstructure is approximated by a constant-mass Dirac Hamiltonian $H = v\sigma \cdot \mathbf{p} + \Delta_g\sigma_3$, where $\Delta_0 \equiv \Delta_K = \Delta_{K'}$ (due to TR symmetry). Berry curvature is then given by the well-known expression

$$\Omega_{\pm,K(K')}(\mathbf{k}) = \mp \frac{\Delta_g v^2 \eta_z}{2\left(v^2\mathbf{p}^2 + \Delta_g^2\right)^{3/2}}, \qquad [11]$$

where $\pm$ refer to the conduction and valence bands and $\eta_z = +$ and $\eta_z = -$ for valley K and K', respectively. This translates into the net Berry curvature flux, which is controlled by the sign of Δ_g:

$$\mathcal{F}_{\mathrm{DP}} = \int d^2k\,\Omega_{\pm,K(K')}(\mathbf{k}) = \mp\pi\eta_z \mathrm{sgn}(\Delta_g), \qquad [12]$$

giving $\mp\pi$ for K, K' valleys, as expected for a Dirac point.

Berry curvature also features hot spots at SBZ corners $\tilde{K}$ and $\tilde{K}'$. These arise from Bragg scattering by the superlattice harmonics in Eq. **2** which mix the pseudospin textures; the energy spectrum and $\Omega(\mathbf{k})$ close to $\tilde{K}, \tilde{K}'$ can be modeled using the $\mathbf{k}\cdot\mathbf{p}$ method; see the *Supporting Information*. We find that the net Berry flux in the conduction band, $\mathcal{F}_{\tilde{K},\tilde{K}'} = \int d^2k\Omega(\mathbf{k})$ about the corners of the SBZ is controlled by m_3,

$$\mathcal{F}_{\tilde{K},\tilde{K}'} = -\frac{\pi}{2}\eta_z \mathrm{sgn}(m_3), \qquad [13]$$

and are equal for both $\tilde{K}$ and $\tilde{K}'$. When m_3 becomes small the hot spots around $\tilde{K}$, $\tilde{K}'$ contract, however the net flux $\pm\pi/2$ for each hot spot remains unchanged.

We note that the "half-Dirac" flux $\pm\pi/2$ follows from Chern number quantization. Integer $\mathcal{C}_v = 1/2\pi\int_{k\in SBZ} d^2k\Omega(\mathbf{k})$ arises from summing the Berry curvature concentrated about DP and $\tilde{K}, \tilde{K}'$ points in the SBZ (as shown in Fig. 3 *A* and *B*). Because there are two inequivalent $\tilde{K}$ points in the SBZ, $\mathcal{C}_v = 1/2\pi(\mathcal{F}_{\mathrm{DP}} + 2\mathcal{F}_{\tilde{K},\tilde{K}'})$. Integer $\mathcal{C}_v$ values and $\mathcal{F}_{\mathrm{DP}} = \pm\pi$ yield $\pm\pi/2$ values for $\mathcal{F}_{\tilde{K},\tilde{K}'}$.

Valley Currents and Berry Curvature Spectroscopy

Topological currents associated with each of the valleys can propagate over extended distances as long as the intervalley scattering is weak (17). Whereas TR symmetry requires no net charge Hall currents, the opposite signs of $\Omega(\mathbf{k})$ in K and K' allow transverse valley currents, $\mathbf{J}_v = \mathbf{J}_K - \mathbf{J}_{K'}$, to be induced by a longitudinal electric field, $\mathbf{E}$. This valley Hall effect (VHE) is described by (6)

$$\mathbf{J}_v = \sigma_{xy}^v \mathbf{E} \times \hat{\mathbf{n}}, \quad \sigma_{xy}^v = \frac{Ne^2}{h}\int \frac{d^2k}{2\pi}\Omega(\mathbf{k})f(\mathbf{k}), \qquad [14]$$

where $\hat{\mathbf{n}}$ points perpendicular to G/*h*BN, $N = 4$ is valley/spin degeneracy, and $f(\mathbf{k}) = (e^{\beta(\epsilon_k - \mu)} + 1)^{-1}$.

The difference between topological bands and nontopological bands is reflected in the behavior of σ_{xy}^v which changes signs as a function of density varying in a single band, or maintains a constant sign, as illustrated in Fig. 3 *C* and *D*. We note that sign-changing σ_{xy}^v does not contradict $\mathcal{C}_v = \pm 1$ for topological bands,

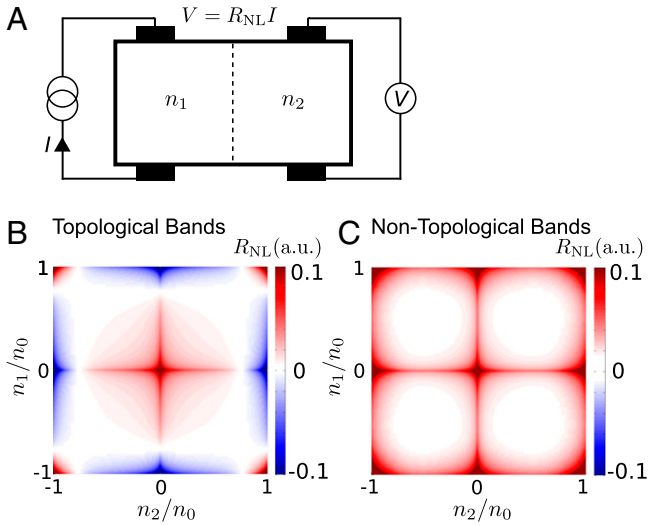

Fig. 4. (*A*) Nonlocal response as an all-electrical diagnostic of the Berry curvature energy dependence and of valley Chern numbers $\mathcal{C}_v$. Shown schematically is an H geometry with separately gated injection and detection regions allowing carrier density n_1, n_2 in these regions to be tuned independently (see the text). (*B* and *C*) The nonlocal resistance $R_{\mathrm{NL}} = A\sigma_{xy}^v(n_1) \times \sigma_{xy}^v(n_2)$ features multiple sign changes as a function of n_1, n_2 for topological bands and no sign changes for nontopological bands. Parameters used are the same as in Fig. 3 *A* and *B*; the corresponding dependence σ_{xy}^v vs. n is shown in Fig. 3 *C* and *D*.

because $\mathcal{C}_v$ tracks the total change in σ_{xy}^v as density is swept through the band. Accounting for a total change of σ_{xy}^v (quantized for topological bands, vanishing for nontopological bands), and using σ_{xy}^v exactly at $\tilde{\Gamma}$ with magnitude $Ne^2/2h$ obtained from counting net Berry flux (19, 20, 29), we obtain the contrasting σ_{xy}^v shown in Fig. 3 *C* and *D*.

Even though the currents $\mathbf{J}_v$ are chargeless, they can be detected by electrical means (8). Indeed, the long propagation lengths enabled by weak intervalley scattering allow valley currents flowing in system bulk to mediate nonlocal electrical response. This is distinct from graphene edge modes that are highly susceptible to localization and gapping out on rough or imperfect edges. In contrast, recent measurements of intervalley scattering in G/*h*BN yield mean-free paths as large as several micrometers (17, 18). Nonlocal resistance measurements (Fig. 4) can therefore provide an all-electrical and robust way to probe the bulk valley-Hall conductivity.

Nonlocal resistance R_{NL} arises in a way illustrated in Fig. 4*A*. Transverse valley currents $\mathbf{J}_v$ induced by an electrical current I can propagate over extended distances to induce a valley imbalance profile across the device, $\delta\mu = \delta\mu_K - \delta\mu_{K'}$. Even far away from the current source, valley imbalance $\delta\mu$ can set up an appreciable transverse electric field via the reverse VHE,

$$\mathbf{E} = \frac{\sigma_{xy}^v(n_2)}{\sigma_{xx}(n_2)}(\nabla\delta\mu)\times\hat{\mathbf{n}}. \qquad [15]$$

This provides a mechanism through which the chargeless long-range valley currents are converted to an electric signal at the readout contacts, producing a nonlocal transresistance R_{NL}. Such R_{NL} was recently observed in ref. 8 for a uniform density device $n_1 = n_2$. Importantly, control over local density in the geometry of Fig. 4*A*, $R_{\mathrm{NL}} = V/I = A\sigma_{xy}^v(n_1)\times\sigma_{xy}^v(n_2)$, is sensitive to the density and signs of σ_{xy}^v in the two regions. Here the prefactor A is positive and depends on the longitudinal conductivity σ_{xx} of both regions, device dimensions, and intervalley scattering length, similar to that analyzed for the spin-Hall effect (30). For illustration, we set $A = (h/e^2)^3$.

Because σ_{xy}^v for topological bands (Fig. 3*C*) changes sign as density is swept in a single band, we find that R_{NL} displays multiple sign changes as a function of density in n_1, n_2 as shown in Fig. 4*B*. The sign-changing behavior of R_{NL} can be traced back to the finite value of $\mathcal{C}_v = \pm 1$ for topological bands and a σ_{xy}^v of $Ne^2/2h$ at neutrality $n_{1,2} = 0$ (i.e., at DP) (19, 20, 30). In contrast, R_{NL} maintains a constant sign for nontopological bands, $\mathcal{C}_v = 0$, as shown in Fig. 4*C*. As a result, sign changes in R_{NL} provide a clear diagnostic for topological bands.

In summary, graphene superlattices provide a practical route to constructing topological bands out of generic materials, as illustrated via tunable electron band topology in commensurate–incommensurate stackings. Band topology can be inferred from nonlocal transport measurements. In addition, interesting behavior is expected in superlattice systems in which large-scale inhomogeneities give rise to topological and nontopological domains. In such systems, domain boundaries are expected to support topologically protected chiral edge states. Transitions between topological and nontopological states can be induced by temperature and strain. A number of different systems can be used, including SiC where superlattice stackings have been observed (31, 32), G/*h*BN (8, 16, 26), and twisted bilayer graphene (33–35). The ease with which stacked G/*h*BN structures can be made (36) and the robust bulk transport signatures of their topological character open the door to accessing and probing electronic band topology in designer topological materials.

ACKNOWLEDGMENTS. This work was supported by National Science Foundation (NSF) Science and Technology Center for Integrated Quantum Materials, NSF Grant DMR-1231319 (to L.S.L.), and in part by the US Army Research Laboratory and the US Army Research Office through the Institute for Soldier Nanotechnologies, under Contract no. W911NF-13-D-0001 (L.S.L.). J.C.W.S. acknowledges support from a Burke Fellowship at Caltech, the Sherman Fairchild Foundation, and a National Science Scholarship.

1. Hasan MZ, Kane CL (2010) Colloquium: Topological insulators. *Rev Mod Phys* 82(4): 3045–3067.
2. Xiao D, Meng MC, Niu Q (2010) Berry phase effects on electronic properties. *Rev Mod Phys* 82(3):1959–2007.
3. Nagaosa N, Sinova J, Onoda S, MacDonald AH, Ong NP (2010) Anomalous Hall effect. *Rev Mod Phys* 82(2):1529–1592.
4. Thouless DJ, Kohomoto M, Nightingale M, den Nijs M (1982) Quantized Hall conductance in a two-dimensional periodic potential. *Phys Rev Lett* 49(6):405.
5. Halperin BI (1982) Quantized Hall conductance, current-carrying edge states, and the existence of extended states in a two-dimensional disordered potential. *Phys Rev B* 25(4):2185.
6. Xiao D, Yao W, Niu Q (2007) Valley-contrasting physics in graphene: Magnetic moment and topological transport. *Phys Rev Lett* 99(23):236809.
7. Mak KF, McGill KL, Park J, McEuen PL (2014) Valleytronics. The valley Hall effect in MoS_2 transistors. *Science* 344(6191):1489–1492.
8. Gorbachev RV, et al. (2014) Detecting topological currents in graphene superlattices. *Science* 346(6208):448–451.
9. Park CH, Yang L, Son YW, Cohen ML, Louie SG (2008) Anisotropic behaviours of massless Dirac fermions in graphene under periodic potentials. *Nat Phys* 4:213–217.
10. Park CH, Yang L, Son YW, Cohen ML, Louie SG (2008) New generation of massless Dirac fermions in graphene under external periodic potentials. *Phys Rev Lett* 101(12):126804.
11. Guinea F, Low T (2010) Band structure and gaps of triangular graphene superlattices. *Philos Trans A Math Phys Eng Sci* 368(1932):5391–5402.
12. Kindermann M, Uchoa B, Miller DL (2012) Zero-energy modes and gate-tunable gap in graphene on hexagonal boron nitride. *Phys Rev B* 86(11):115415.
13. Wallbank JR, Patel AA, Mucha-Kruczynski M, Geim AK, Fal'ko VI (2013) Generic miniband structure of graphene on a hexagonal substrate. *Phys Rev B* 87(24):245408.
14. Song JCW, Shytov AV, Levitov LS (2013) Electron interactions and gap opening in graphene superlattices. *Phys Rev Lett* 111(26):266801.
15. Yankowitz M, et al. (2012) Emergence of superlattice Dirac points in graphene on hexagonal boron nitride. *Nat Phys* 8:382–386.
16. Woods CR, et al. (2014) Commensurate-incommensurate transition in graphene on hexagonal boron nitride. *Nat Phys* 10:451–456.
17. Gorbachev RV, Tikhonenko FV, Mayorov AS, Horsell DW, Savchenko AK (2007) Weak localization in bilayer graphene. *Phys Rev Lett* 98(17):176805.
18. Cuoto NJG, et al. (2014) Random strain fluctuations as dominant disorder source for high-quality on-substrate graphene devices. *Phys Rev X* 4(4):041019.
19. Li J, Morpugo AF, Büttiker M, Martin I (2010) Marginality of bulk-edge correspondence for single-valley Hamiltonians. *Phys Rev B* 82(24):245404.
20. Jung J, Zhang F, Qiao Z, MacDonald AH (2011) Valley-Hall kink and edge states in multilayer graphene. *Phys Rev B* 84(7):075418.
21. Kane CL, Mele EJ (2005) Quantum spin Hall effect in graphene. *Phys Rev Lett* 95(22): 226801.
22. Weeks C, Hu J, Alicea J, Franz M, Wu R (2011) Engineering a robust quantum spin Hall state in graphene via adatom deposition. *Phys Rev X* 1(2):021001.
23. Cooper NR (2011) Optical flux lattices for ultracold atomic gases. *Phys Rev Lett* 106(17):175301.
24. San-Jose P, Gutiérrez A, Sturla M, Guinea F (2014) Electronic structure of spontaneously strained graphene on hexagonal boron nitride. *Phys Rev B* 90(11):115152.
25. Jung J, DaSilva A, MacDonald AH, Adam S (2014) Ab initio theory of moiré superlattice bands in layered two-dimensional materials. *Phys Rev B* 89(20):205414.
26. Hunt B, et al. (2013) Massive Dirac fermions and Hofstadter butterfly in a van der Waals heterostructure. *Science* 340(6139):1427–1430.
27. San-Jose P, Gutiérrez A, Sturla M, Guinea F (2014) Spontaneous strains and gap in graphene on boron nitride. *Phys Rev B* 90(7):075428.
28. Fukui T, Hatsugai Y, Suzuki H (2005) Chern numbers in discretized Brillouin zone: Efficient method of computing (spin) Hall conductances. *J Phys Soc Jpn* 74:1674.
29. Lensky YD, Song JCW, Samutpraphoot P, Levitov LS (2015) Topological valley currents in gapped Dirac materials. *Phys Rev Lett* 114(25):256601.
30. Abanin DA, Shytov AV, Levitov LS, Halperin BI (2009) Nonlocal charge transport mediated by spin diffusion in the spin Hall effect regime. *Phys Rev B* 79(3):035304.
31. Berger C, et al. (2006) Electronic confinement and coherence in patterned epitaxial graphene. *Science* 312(5777):1191–1196.
32. Zhou SY, et al. (2007) Substrate-induced bandgap opening in epitaxial graphene. *Nat Mater* 6(10):770–775.
33. Li G, et al. (2010) Observation of Van Hove singularities in twisted graphene layers. *Nat Phys* 6:109–113.
34. Luican A, et al. (2011) Single-layer behavior and its breakdown in twisted graphene layers. *Phys Rev Lett* 106(12):126802.
35. Sanchez-Yamagishi JD, et al. (2012) Quantum Hall effect, screening, and layer-polarized insulating states in twisted bilayer graphene. *Phys Rev Lett* 108(7):076601.
36. Dean CR, et al. (2010) Boron nitride substrates for high-quality graphene electronics. *Nat Nanotechnol* 5(10):722–726.